Jordan Journal of Physics

ARTICLE

Fabrication and Performance Testing of Composite Molybdenum: "Resinpal 2301" Field Emission Emitters

Amer Z. Ma'ni[a], **Mohammad M. Allaham**[b,c], **Mohammad H. Alsa'eed**[a], **Alexandr Knápek**[c], **Saad S. Alrwashdeh**[a] and **Marwan S. Mousa**[a]

[a] *Department of Physics, Mu'tah University, Al-Karak 61710, Jordan.*
[b] *Central European Institute of Technology, Brno University of Technology, Purkyňova 123, 612 00 Brno, Czech Republic.*
[c] *Institute of Scientific Instruments of Czech Academy of Sciences, Královopolská 147, 612 64 Brno, Czech Republic.*

Abstract: Over the past few decades, epoxy resins have shown several advantages as coating materials for field emission electron sources; this includes lowering the operation applied voltages and the threshold voltage required to start the electron emission process. This study illustrates the results of using the Resinpal 2301 epoxy resin as a coating material for field emission emitters. The results include the ultraviolet photoelectron spectroscopy analysis to obtain an average value for the local work function and ionization energy for the cured coating layer. The samples were checked using scanning electron microscopy before and after being coated with the cured epoxy resin. Moreover, the field emission microscopy characteristics of both uncoated molybdenum and composite molybdenum-epoxy samples are presented in the form of a comprehensive comparison. The study shows promising results in enhancing the field emission characteristics with the application of the coating material. Notably, there was a significant reduction in the threshold voltage. The emission current values from coated samples were found to be at least ~11 times higher than those from uncoated samples.

Keywords: Field electron emission, Composite electron sources, Resinpal 2301, Molybdenum emitters, Molybdenum-epoxy composite.

1. Introduction

In metals, the local work function is the difference in energy between the vacuum level and the Fermi level of a metal. In the context of field emission theory, the vacuum level is considered at the top of the metal's conduction band, while the Fermi level is located at the top of its valence band. This work function forms the surface potential energy barrier (PEB) [1, 2]. When metals are under the influence of an intense electrostatic field (~ 3 V/nm), the surface potential barrier is reduced to an image rounded-PEB [3, 4]. Even at low temperatures, such as room temperature where electrons' energy does not exceed 0.026 eV above the Fermi level, this process helps cold electrons to tunnel through the reduced PEB to vacuum. This mechanism is well-known as the cold field emission of electrons (CFE). The emitted electrons are then electrically accelerated within the separation space between the two electrodes forming an electron beam [5].

In regular CFE experiments, the relationship between the measured applied voltage V_m and the emission current I_m is expressed by the extended Murphy-Good equation [6]. This equation describes the current-voltage characteristics $\left(I_m(V_m)\right)$ in the following form [7]:

$$I_m = A_f^{SN} \exp(\eta)\, \theta V_{mR}^{-\kappa} V_m^{\kappa} \exp(-\eta V_{mR} V_m^{-1}) \quad (1)$$

In Eq. (1), A_f^{SN} is the formal emission area through the image rounded-PEB (or the Schottky-Nordheim (SN-PEB), where $\eta(\phi) = bc_S^2\phi^{-1/2}$ and $\theta(\phi) = ac_S^{-4}\phi^3$ are scaling parameters. Here, a and b, are the first and second Fowler-Nordheim constants, c_S is the Schottky constant, ϕ is the local work function, V_{mR} is a reference measured voltage used to describe the maximum applied voltage that should not be exceeded to stay within the limits of the cold field emission regime, and $\kappa = 2 - \eta/6$ is the pre-exponential factor of the Murphy-Good analysis plot [3, 6, 7].

The Murphy-Good (MG) analysis method is a mathematical interpretation of the $I_m(V_m)$ in a nearly exact linear form. An MG-plot takes the form $\ln(I_m/V_m^{\kappa})$ vs V_m^{-1}. Using the notations $L_{MG} = \ln(I_m/V_m^{\kappa})$ for the vertical axis and $x = V_m^{-1}$ for the horizontal axis, the theoretical form of MG-plots takes the following form [7–11]:

$$L_{MG} = \ln\left(A_f^{SN}\exp(\eta)\,\theta V_{mR}^{-\kappa}\right) - \eta V_{mR}x \quad (2)$$

The slope of Eq. (2) is used to extract an average value for V_{mR}, which in turn is used to derive a useful parameter known as the characteristic scaled field ($f_C = V_m/V_{mR}$). The scaled field values are important for applying the Forbes field emission orthodoxy test (FOT). The FOT test is important to validate the prepared samples before coating, which is important to proceed with the experiment. This can be done by checking whether the experiment was operated in an orthodox field emission regime or not [12, 13].

Moreover, in FOT theory, the extracted f_C limits from an analysis graph are compared to a range of limits found in trusted literature for a set of work functions. If the extracted limits are located within the orthodox range, then the extracted values for the characterization parameters are considered valid, and the experiment is done within the cold field emission regime. If any of the limits are located outside the range, it is advisable not to consider the values of the characterization parameters since the experiment would not be within the cold field emission regime.

Coating metal cathodes with insulating thin layers has been found to be a promising and useful technique in CFE experiments. This form of composite single-tip field emitters features a metal-insulator-vacuum interface and has been in use since the early 1980s. Several types of vacuum-friendly insulating materials, such as various oxides or epoxy resins, can be employed in this technique [14–18]. The existence of such a layer changes the entire characteristics of CFE behavior, resulting in a more focused and intense electron beam, much lower threshold voltage, and higher macroscopic emission current densities [19–21]. This change in characteristics is believed to happen due to a change from the cold field emission regime to the thermionic-field emission regime at room temperatures [22].

In this study, the CFE characteristics of both uncoated and coated single-tip field molybdenum (Mo) emitters are introduced. The coating material is Resinpal 2301 epoxy resin, with polycrystalline molybdenum as the base metal. The study includes ultraviolet photoelectron spectroscopy (UPS) analysis for the cured coating layer, field emission microscope (FEM) $I_m(V_m)$, FEM macroscopic emission current density distribution patterns, and scanning electron micrographs (SEMs). The UPS analysis is used to evaluate an average value for the cured Resinpal 2301 local work function, which is important for obtaining the MG-analysis plots.

2. Materials and Methodology

2.1 Materials

In this study, we choose Mo because of its advantageous properties such as electron work function of 4.27 eV, hardness of 5–6 on the Mohs scale, and a high melting point of 2620 °C [23]. The drop-off electrochemical etching technique was used to obtain different profile shapes and tip radii of Mo emitters. Annealed Mo wire segments of 99.95% in purity, 1.5 cm in length, and 0.1 mm in diameter, were prepared, straightened, and connected to the anode of a special etching instrument, the Armin-m etching/coating device [24].

The etchant of the Mo wires was a (5:1 methanol-sulfuric acid solution, which was left to cool down in an ice bath for 60 minutes. To start the etching procedure, the etching voltage was fixed at 12 V. This fixed voltage, along with a consistent concentration of the etching solution, helps produce homogeneous samples in terms of tip profile shape and diameter.

The attached sample was then vertically immersed in the etching solution, with the immersed part not exceeding a length of 2 mm. During the etching process, the gradual decrease in electric current was monitored by an ammeter until a sudden drop indicated the end of the etching process. The prepared sample was quickly withdrawn from the solution to prevent losing its apex. Finally, the produced samples were cleaned in an ultrasonic distilled water bath for 9 minutes.

Resinpal 2301 is a standard high-quality two-component epoxy resin from Resinpal, Germany, primarily used in coatings. This medium-reactive epoxy resin is characterized by low exothermicity, maximum strength, low shrinkage, and high resistance to other chemicals (check the technical documentation for more details).

To prepare the coating layer, a 2:1 laminate of Resinpal 2301 epoxy resin and epoxy hardener was prepared in a container. The laminate was left to cure for one hour before starting the coating process. Then, each sample tip was dipped into the cured laminate until a noticeable layer of the resin formed. The samples were left for 24 hours until the resin hardened on the apex of the tip.

2.2 Experimental Setup

The AXIS Supra^{TM} X-ray photoelectron spectrometer setup (KRATOS Analytical Ltd., Manchester, UK) was used for the UPS analysis. The spectra acquisition step size was set to 0.025 eV and five sweeps were performed. The UPS photon energy was acquired from the He I lamp with a photon energy of 21.22 eV. This energy was used to excite the sample surface to evaluate the average local work function and the ionization potential of a cured epoxy layer.

To obtain high-magnification SEMs at higher resolutions, the samples were checked using an FEI ESEM Quanta 450 FEG scanning electron microscope. This SEM is a multi-purpose scanning electron microscope that has three imaging modes: high vacuum mode (for conventional SEM use), low vacuum mode (for imaging nonconductive samples without conductive layer coatings), and environmental SEM (ESEM) mode (for imaging wet samples or samples in a gaseous environment inside the imaging chamber). This instrument uses a thermally assisted field emission electron source (or electron gun), known as a Schottky cathode. After imaging the samples in the SEM, they were transferred to the field emission microscope to study their field emission characteristics.

A traditional FEM was used to study the field emission characteristics (see Fig. 1 for the FEM schematics). This FEM includes an ultra-high vacuum chamber connected to a silicon oil diffusion pump, a sample holder, and an imaging screen. The chamber contains a liquid nitrogen cooling trap and is covered by an electrical heating system to help in the pumping process. This traditional FEM has distinctive features, such as the ability to test four samples in one experiment and the ability to heat and cool the vacuum chamber, which is useful to increase the vacuum.

In this setup, the samples were connected to a high-voltage power supply (FUG HCN140-6500), that can operate up to 6.5 kV. The high voltage is supplied to the samples through a protective high resistor (140 MΩ) to ensure the safety of the setup and protect the samples from exploding when subjected to high electrical currents.

The imaging screen in this setup is composed of a glass screen coated with a transparent layer of conductive tin oxide (SnO_2), followed by a thin layer of phosphorus. The phosphorus is important because it interacts with the incident electrons, providing a photon for each electron absorbed. This process allows us to capture a live image of the emission current distribution. These images, called field emission microscope patterns, have several advantages and important roles in field emission studies, such as imaging the macroscopic emission current density distributions and the emission current stability.
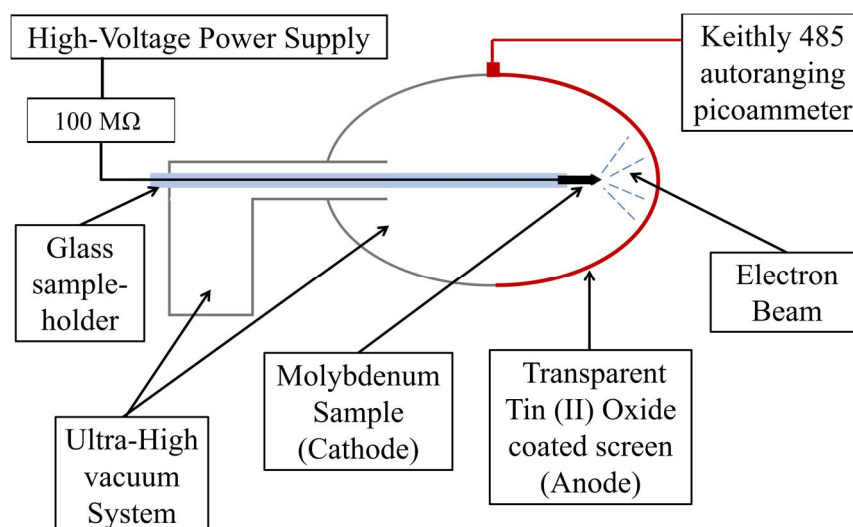
FIG. 1. A schematic diagram of the field emission microscope setup.

To complete the circuit, the phosphorus imaging screen is connected to a grounded picoamperemeter (KEITHLEY 485 auto-ranging picoammeter). The picoamperemeter is used to record the emission current values at each applied voltage value. This is useful for creating the $I_m(V_m)$ characteristics and studying the emission process using a suitable analysis method.

The setup contains a high vacuum system that provides a gas pressure of ~5×10⁻⁶ mbar without any extra operations. The system is composed of a silicon oil diffusion pump [19, 20]. When the pump is heated, the silicon oil evaporates and condenses in the upper parts of the pump, collecting the gas atoms and molecules. When the oil molecules are cooled and condensed, they drop down, carrying the gas molecules with them to the exit line, which is connected to a rotary pump that removes the molecules from the system.

To improve the quality of the vacuum level, the chamber is covered by heating tapes that are totally isolated to heat the system. The heating process is carried out overnight for 12 hours until the measured temperature of the chamber surface is about 390 K. At this point, the heating system is turned off, and liquid nitrogen is filled inside the trap to provide quick cooling for the system, which helps to reduce the gas pressure to ~2×10⁻⁷ mbar.

3. Results and Discussion

3.1 Characteristics of Resinpal 2301 Epoxy Resin

To evaluate an average local work function value for the Resinpal 2301 epoxy resin, thin films of thickness 0.1 mm were prepared on glass sheets. First, the XPS analysis was conducted while activating charge neutralizer settings with a filament current of 0.45 A, a filament bias of 1.05 V, and a charge balance of 4.6 V. The emission current was set to 15 mA, and three sweeps were carried out for each measurement. The results, presented in Fig. 2, show that the main elements of the Resinpal 2301 epoxy resin are carbon, oxygen, nitrogen, silicon, and a very small peak of chlorine.

The main results obtained were from the UPS analysis. The experiments were carried out under the same charge neutralizer conditions as the XPS measurements. The He I ultraviolet source was used with a photon energy of 21.22 ± 0.12 eV. The results, presented in Fig. 3, show that the secondary electron cut-off energy (E_{SECO}) was 18.3 eV, and the Fermi level (E_F) was located around 0.33 eV. The top of the highest occupied molecular orbital (E_{HOMO}) was located at 1.88 eV. Using this information we applied the following two equations to determine the work function and ionization potential of the epoxy resin [25]:

$$\phi = h\upsilon - E_{SECO} - E_F \qquad (3)$$

$$I.P. = \phi + E_{HOMO} \qquad (4)$$
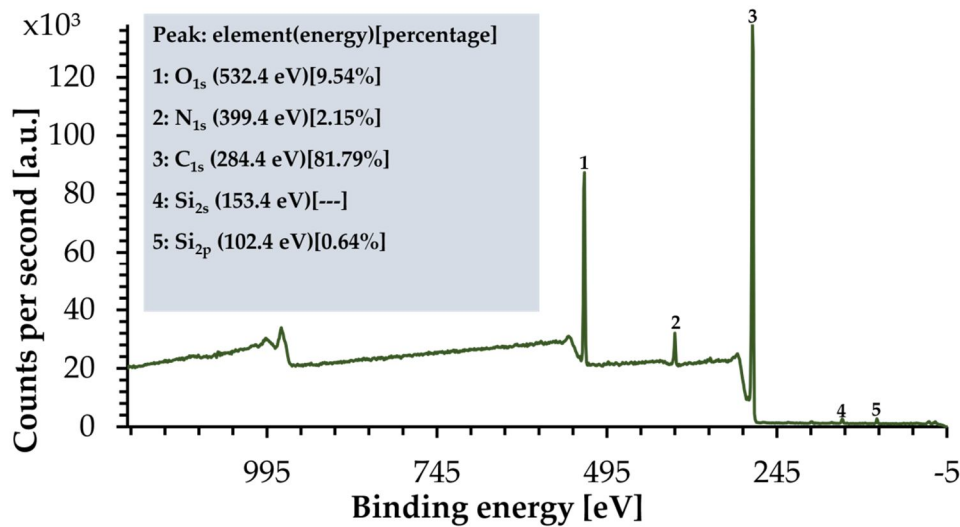
FIG. 2. The XPS results for the Resinpal 2301 epoxy resin.
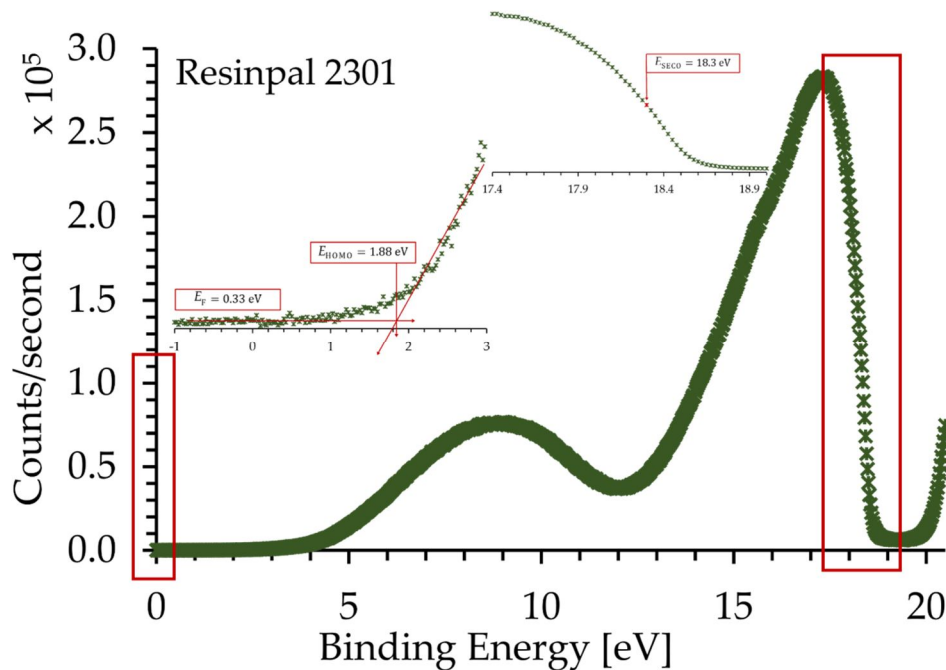
FIG. 3. The UPS analysis results for the Resinpal 2301 epoxy resin.

The average local work function of the cured epoxy was $\phi = 2.59 \pm 0.12$ eV, and the ionization potential was $I.P. = 4.47 \pm 0.12$ eV. This information is extremely important for analyzing the results for the composite samples because the electrons are emitted from the coating layer, not the surface of Mo.

3.2 Geometrical Characteristics of the Fabricated Emitters

This section includes the results obtained from two Mo samples, tagged Mo_1 and Mo_2.

After producing the samples by the etching process, the validity of the tip apex was checked using the Leica DVM6 visible light microscope before proceeding with the experiment. The obtained images are presented in Fig. 4.

After checking the produced samples with the visible light microscope, the samples were transferred to the Quanta 450 FEG scanning electron microscope. The obtained SEM images for the two samples are presented in Fig. 5.
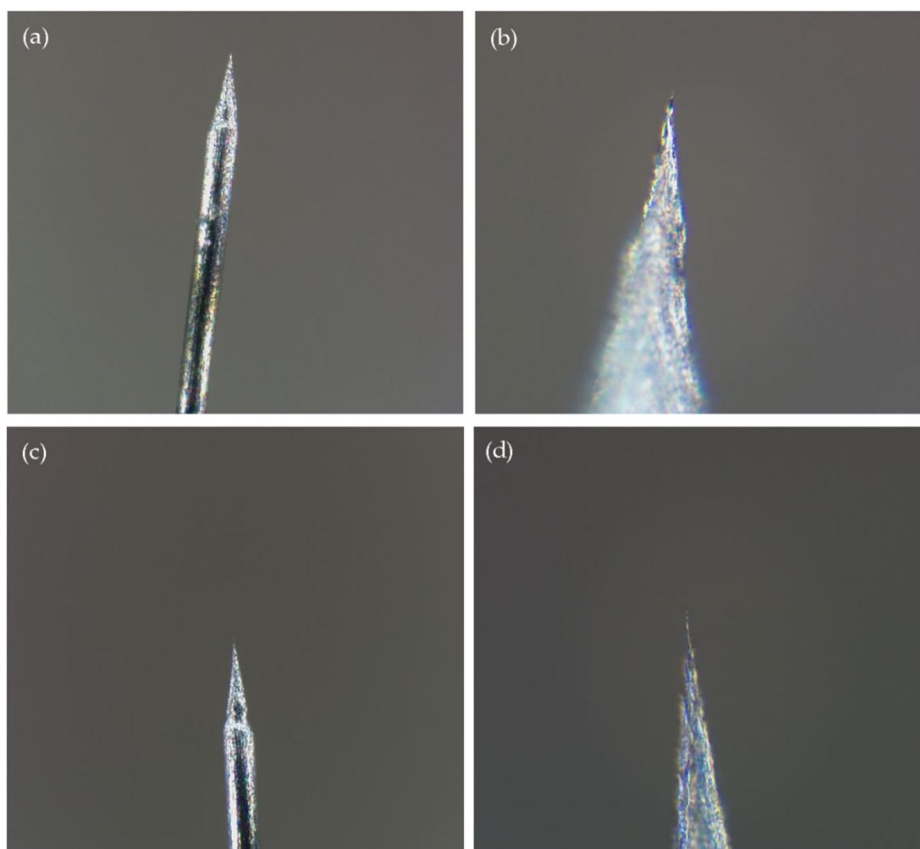
FIG. 4. The visible light microscope image for (a) Mo_1 sample at 360 × magnification, (b) Mo_1 sample at 5911 × magnification, (c) Mo_2 sample at 418 × magnification, and (d) Mo_2 sample at 5890 × magnification.
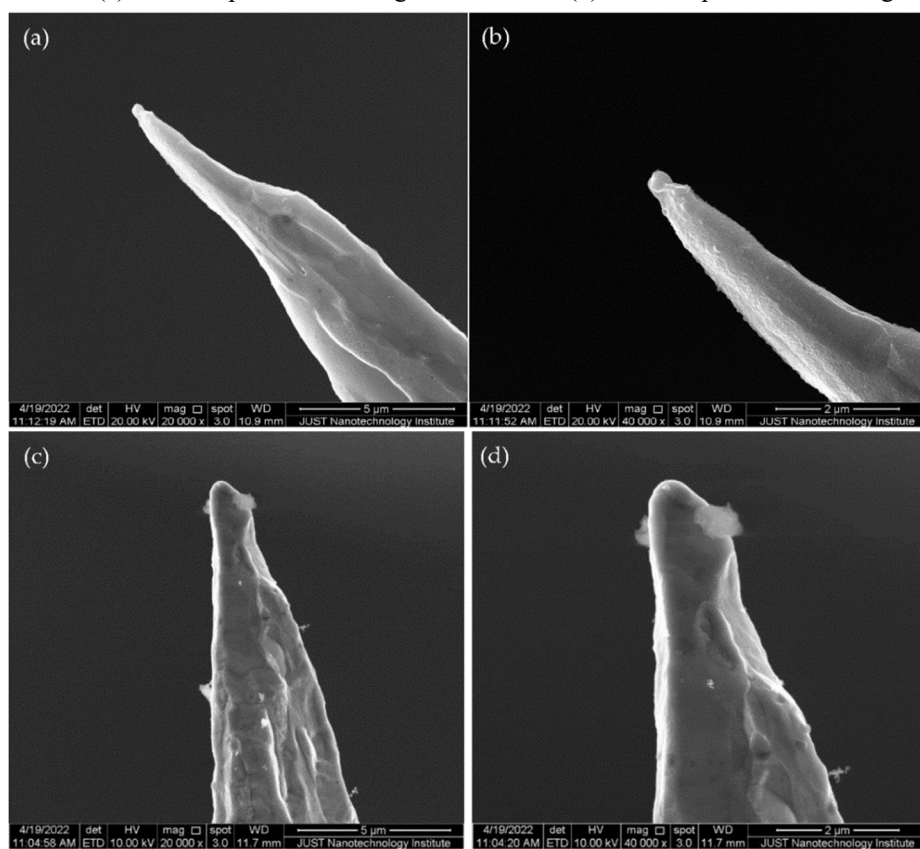
FIG. 5. Scanning electron micrograph for the uncoated (a) Mo_1 sample at a magnification of 20000 ×, (b) Mo_1 at a magnification of 40000 ×, (c) Mo_2 sample at a magnification of 20000 ×, and (d) Mo_2 sample at a magnification of 40000 ×.

The same procedure for checking the uncoated samples was applied to the coated Mo samples. The number of dips applied for each sample was as follows: Mo_1 has a layer formed by dipping the apex into the epoxy three times, while Mo_2 has a layer formed from six dips. The approximate thickness of each layer was measured by subtracting the curvature radius of the uncoated tip from the curvature radius of the coated tip. The approximate curvature radii were determined in-situ during the SEM measurement of the coated samples. The results were used to determine the thickness of the coated samples as presented in Fig. 6.
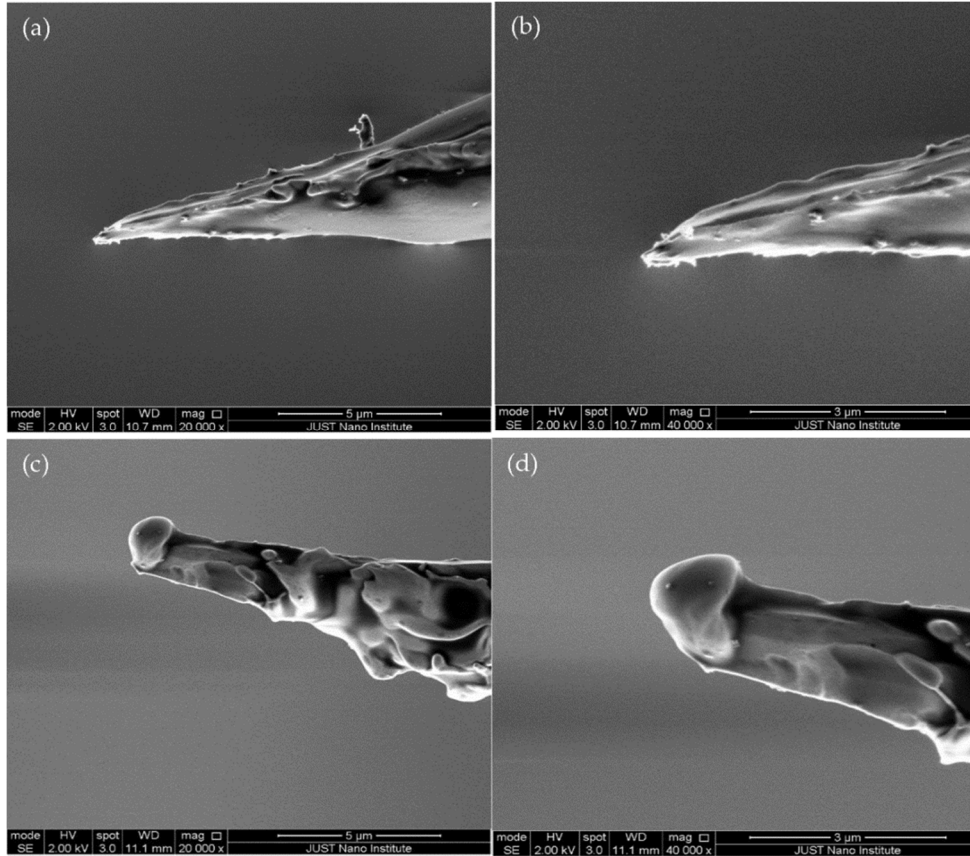
FIG. 6. Scanning electron micrograph for the coated (a) Mo_1 sample at a magnification of 20000 ×, (d) Mo_1 at a magnification of 40000×, (c) Mo_2 sample at a magnification of 20000 ×, and (d) Mo_2 sample at a magnification of 40000 ×.

The measured curvature radii (before and after coating) and the related thickness values as obtained for each sample are summarized in Table 1.

TABLE 1. The radii of the uncoated samples (superscript "un"), the coated samples (superscript "co"), and the thickness of the coating layer for each sample.

Sample index Mo_i	Number of dips	R_i^{un} [nm]	R_i^{co} [nm]	Thickness d_i [nm]
Mo_1	3	54	178	124
Mo_2	6	127	748	621

3.3 Field Emission Characteristics

The obtained FEM results include the FEM pattern images, which describe the distribution of the emitted current density. These patterns are magnified images of the emission regions from the surface of the tip apex. In addition to these images, the set-up is prepared to collect the $I_m(V_m)$ and the related analysis plots. This is useful to check the validity of the uncoated tips after finishing the experiment before proceeding with the next steps, which can be verified through the analysis process.

For the composite samples, the results are divided into two parts. The first part deals with the results of the switch-on phenomenon (sudden appearance of the emission current at relatively

high values). This part includes the recorded FEM patterns along with the $I_m(V_m)$ and its logarithmic scale. The second part includes the usual FEM pattern images, the $I_m(V_m)$, and the MG analysis plots for a full cycle.

3.3.1 Field Emission Characteristics of Mo$_1$ Sample

The FEM pattern images are presented in Fig. 7. The images were captured at different $I_m(V_m)$ values during both the increasing part of the applied voltages [Figs. 7(a)-7(d)] and the decreasing part [Figs.7(d)-7(f)]. These images show how current density increases as the applied voltage rises, evident in the brighter, more dispersed patterns on the screen.

As seen in SEMs in Figs. 5 and 6, the samples' surfaces contain some residues from the etchant solution and additional particles possibly accumulated during the transportation process. To get rid of this contamination, the applied voltage is increased gradually over several cycles in all experiments. The first cycle is a degassing cycle, which is important for cleaning the surface of the sample apex. During this cycle, the $I_m(V_m)$ is not considered because

it contains highly fluctuated results with no useful information.

During the second cycle of the experiment, $I_m(V_m)$ and related MG-plots were obtained for the two parts, as shown in Fig. 8. The pre-exponential factor for the MG-plots was calculated using a web-based field emission analysis software [23], the results were tested by the orthodoxy test with extraction performed using the same analysis software. The results are presented in Table 2.

As observed in Figs. 7(a) and 8(a), the emission process started at an applied voltage of 1080 V, initially appearing as a tiny dot near the screen center in the FEM pattern. This dot then enlarged as the applied voltage increased, as shown in Figs. 7(a)-7(d). The $I_m(V_m)$ characteristics in Fig. 8(a) show how the macroscopic emission current density increased and spread with increasing applied voltage. Moreover, during voltage reduction, the FEM pattern size shrank, as seen in Figs.7(e)-7(f), accompanied by a reduction in emission current as predicted by MG theory.
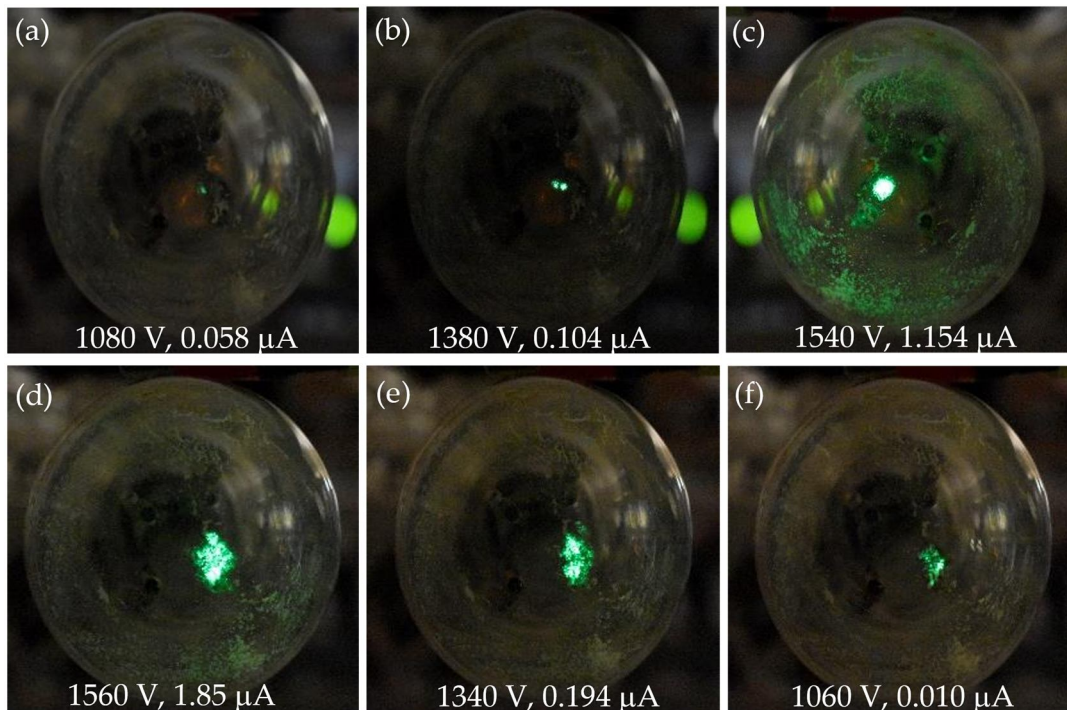
FIG. 7. FEM pattern images for the sample Mo$_1$ that describe the macroscopic emission current density distribution. The images were captured at different current-voltage data as presented in each part (a) – (f).
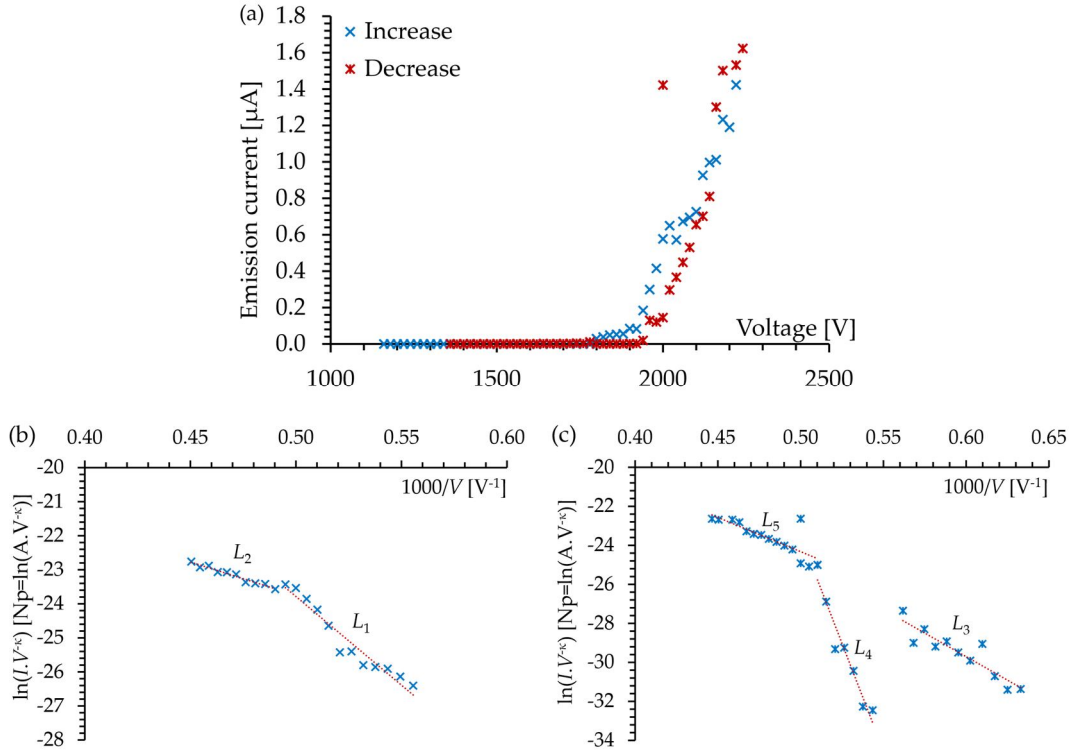
FIG. 8. The obtained (a) current-voltage characteristics for a full applied voltage cycle for the sample Mo_1, and the Murphy-Good plots for the (b) increasing and (c) decreasing parts of the cycle.

TABLE 2. Field emission orthodoxy test and field emission analysis results for the Mo_1 sample.

Segment index L_i	f_c		Test result	A_f^{SN} [m²]	ζ_c [nm]
	f_c^{low}	f_c^{up}			
L_1	0.15	0.20	Pass	2.5×10^{-11}	815.3
L_2	0.48	0.52	Inconc.	4.5×10^{-18}	337.9
L_3	0.13	0.15	Pass	1.4×10^{-9}	950.4
L_4	0.04	0.04	Fail	N/A	N/A
L_5	0.25	0.29	Pass	1.7×10^{-14}	615.1

The MG-analysis plot for the increasing part of the applied voltage cycle is presented in Fig. 8(b). It shows a kinked plot that forms two segments labeled L_1 and L_2. Analysis results for these two segments are presented in Table 2. The L_1 segment passed the orthodoxy test, which means it operated within a suitable voltage interval without causing any significant changes to the surface of the emitter apex, chemical composition, or geometry. The L_2 segment had an inconclusive result because the upper limit scaled field value shows higher operation voltage than what is required.

The analysis plot for the decreasing part of the applied voltage cycle is presented in Fig. 8(c). The plot contains three segments, L_3, L_4, and L_5. L_3 and L_5 exhibit nearly identical slopes and pass the orthodoxy test, as presented in Table 2. As for L_4, it shows a difference in the slope line segment, which is believed to be related to the creation and elimination of another emission spot that was generated during the voltage decrease, as evidenced by its specific starting and ending points within the plot. The orthodoxy test showed a failed result which is expected for such side events during the emission process.

In addition to these results, Table 2 shows a large emission area in the range of squared micrometers and large voltage conversion lengths for the pass segments. Such results are important for future studies that are related to the behavior of the emitted electron beams.

For the composite Mo_1 sample, the switch-on phenomenon was observed and recorded at an applied voltage of 5600 V with an emission current of 17.11 μA. These values are known as the switch-on voltage V_{SW} = 5600 V and the

switch-on current I_{SW} = 17.11 µA. The related switch-on pattern is presented in Fig. 9(a). The applied voltage was then slowly reduced, and the $I_m(V_m)$ was recorded, as shown in Fig. 10(a), along with its logarithmic scale, presented in Fig.10(b). The logarithmic scale of the $I_m(V_m)$ is important in the case of the switch-on cycle

because it shows how the current is saturated at its maximum value.

During this cycle, the emission process turned off at a voltage known as the threshold voltage V_{TH}, which for this sample was recorded at 300 V with a threshold current I_{TH} of 0.05 µA.
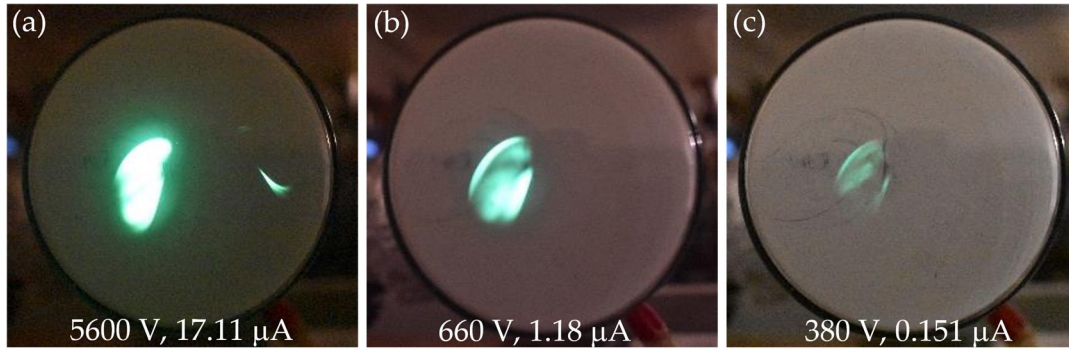
FIG. 9. FEM pattern images for the coated Mo$_1$, (a) describes the switch-on pattern where the switch-on voltage was 5600 V with the switch-on current value of 17.11 µA. Images (b) – (c) describe the pattern at different applied voltages and current values.
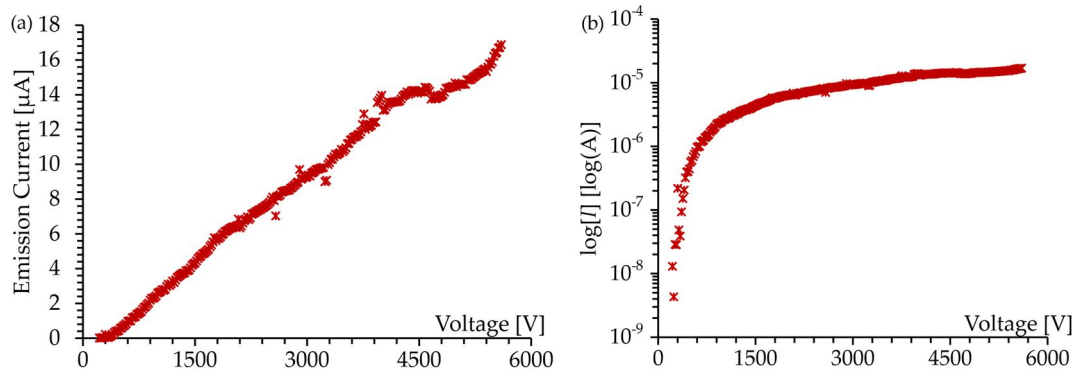
FIG. 10. The obtained (a) current-voltage characteristics for the switch-on decreasing part of the applied voltages for the coated Mo$_1$, and (b) the logarithmic scale for emission current values in amperes.

After finishing the switch-on cycle, an increasing/decreasing cycle for the applied voltage was performed. For this sample, the FEM pattern images are presented in Fig. 11, and its $I_m(V_m)$ is presented in Fig. 12(a). As seen in Fig. 11(a), the first emission pattern was observed at 280 V with an emission current of 0.103 µA. The applied voltage was then increased to 800 V, where the recorded current was 3.22 µA. When the voltage reached 800 V, the decreasing part of the cycle was performed. The threshold voltage was recorded at V_{TH} = 180 V with an emission current I_{TH} = 0.065 µA.

The MG-analysis plot of the voltage-increasing part is presented in Fig. 12(b). The plot contains five segments connected in series

($L_6 - L_{10}$), and their analysis results are presented in Table 3. As expected, only low-field regions had inconclusive results with extremely low emission areas and voltage conversion lengths. The rest failed the orthodoxy test because the emission process took place in a non-orthodox field emission regime. The MG-plot for the voltage-decreasing part is presented in Fig. 12(c). The plot consists of two segments L_{11} and L_{12}. During the voltage-decreasing part, the emission process was more stable since the primary segment L_{11} does not have kinked behavior. However, another emission spot was created in the range of 400–312 V, leading to a failed result as expected (segment L_{12}).
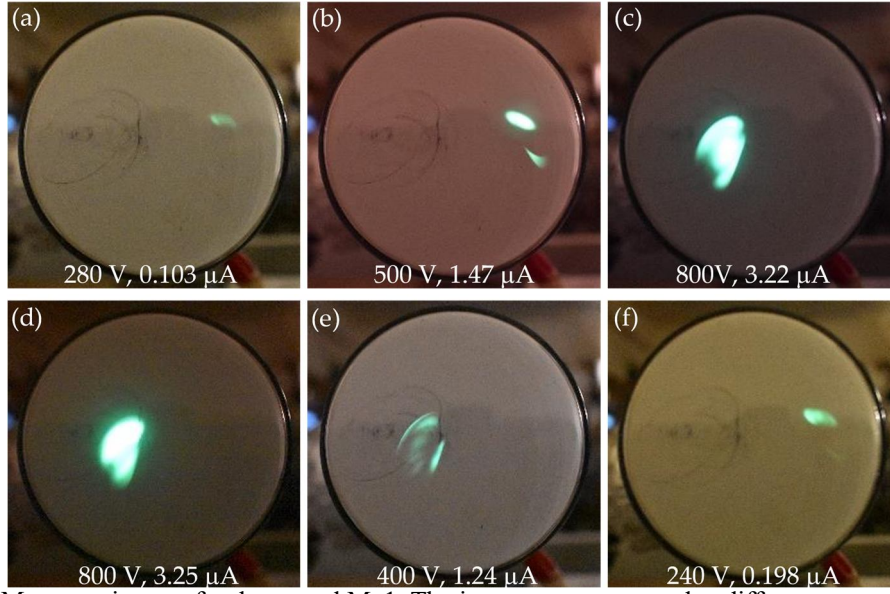
FIG. 11. FEM pattern images for the coated Mo1. The images were captured at different current-voltage data presented in each part (a)-(f).
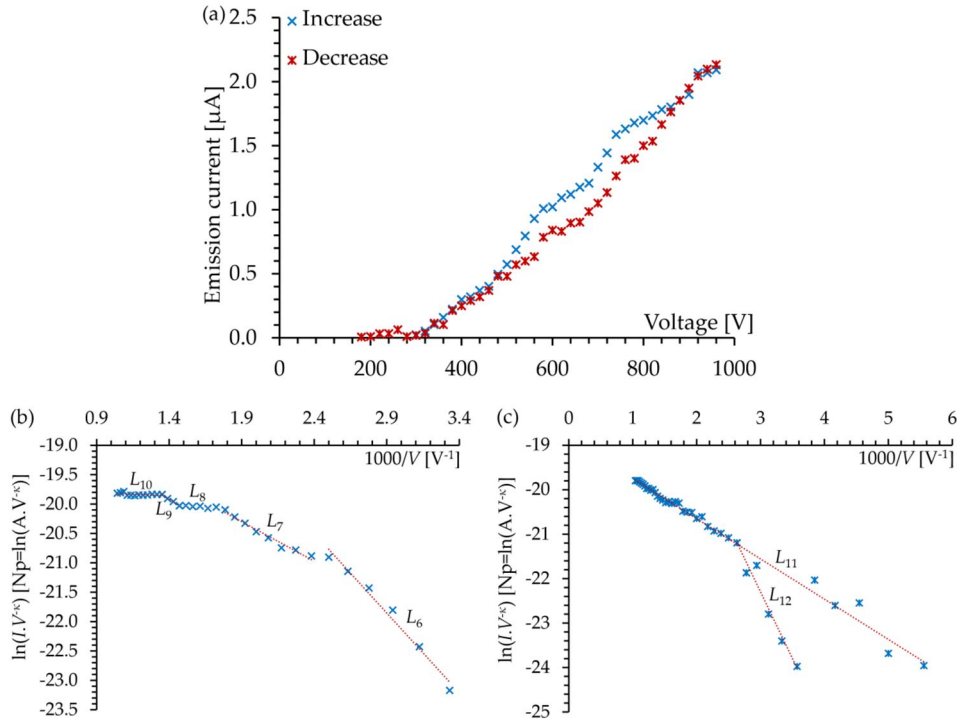
FIG. 12. The obtained (a) current-voltage characteristics for a full applied voltage cycle for the sample coated Mo_1, and the Murphy-Good plots for the (b) increasing and (c) decreasing parts of the cycle.

TABLE 3. Field emission orthodoxy test and field emission analysis results for the coated Mo_1 sample.

Segment index L_i	f_c		Test result	A_f^{SN} [m²]	ζ_c [nm]
	f_c^{low}	f_c^{up}			
L_6	0.67	0.90	Inconc.	5.1×10^{-20}	95.6
L_7	1.95	2.60	Fail	N/A	N/A
L_8	15.50	18.83	Fail	N/A	N/A
L_9	2.59	2.82	Fail	N/A	N/A
L_{10}	67.18	87.15	Fail	N/A	N/A
L_{11}	1.19	6.37	Fail	N/A	N/A
L_{12}	0.58	0.79	Inconc.	1.1×10^{-19}	103.9

The reason behind the failed results for the composite samples can be clearly seen from the extracted scaled field values in Table 3. The inconclusive results have reasonable values ($f_C^{extr} < 1$), while the extracted results for the failed samples were much higher than one. Thus, this type of field emission emitters still requires more study.

Generally, in the case of composite emitters, the expected results of the orthodoxy test are likely to fail. This is because the orthodoxy test is designed to provide evidence of how the emission process operated within well-studied conditions found in the literature. However, this is not the case with composite emitters, since there are no suitable orthodoxy testing criteria

yet. The results included in this study serve as preliminary studies of such emitters.

3.3.2 Field Emission Characteristics of Mo₂ Sample

For this sample, the switch-on phenomenon was observed and recorded at an applied voltage of V_{SW} = 5600 V, where the switch-on current was I_{SW} = 16.9 µA. The switch-on FEM pattern is presented in Fig. 13(a). The applied voltage was then slowly reduced, and the $I_m(V_m)$ was recorded. These values are presented in Fig. 14(a), along with their logarithmic scale shown in Fig. 14(b). After finishing the first voltage decrease cycle, the threshold voltage was recorded at V_{TH} = 390 V with a threshold current I_{TH} = 0.04 µA. Note that the logarithmic scale in this case shows a more saturated current.
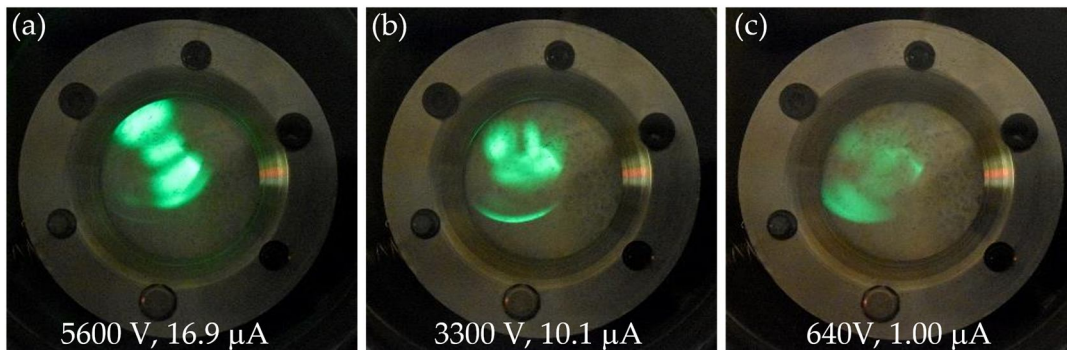
FIG. 13. FEM pattern images for the sample coated Mo₂. Image (a) shows the switch-on pattern where the switch-on voltage was 6000 V with the switch-on current value of 29.0 µA. Images (b)–(c) depict the pattern at different applied voltages and current values.
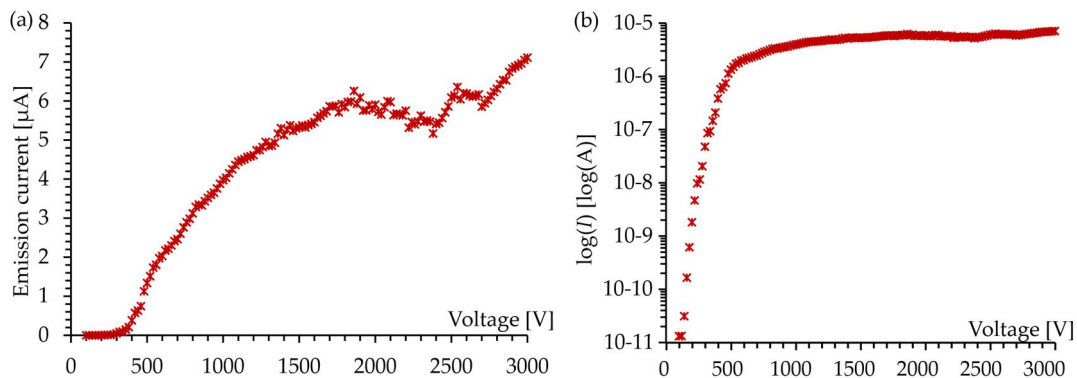
FIG. 14. (a) Current-voltage characteristics for the switch-on decreasing part of the applied voltages for the coated Mo₂ and (b) the logarithmic scale for emission current values in amperes.

An increase/decrease cycle for the applied voltage was then performed. The obtained FEM pattern images are presented in Fig. 15, and its $I_m(V_m)$ is shown in Fig. 16(a). As seen in Fig.

15(a), the first emission pattern was observed at 320 V with an emission current of 0.25 µA. The applied voltage was then increased up to 960 V, where the recorded current was 2.09 µA.
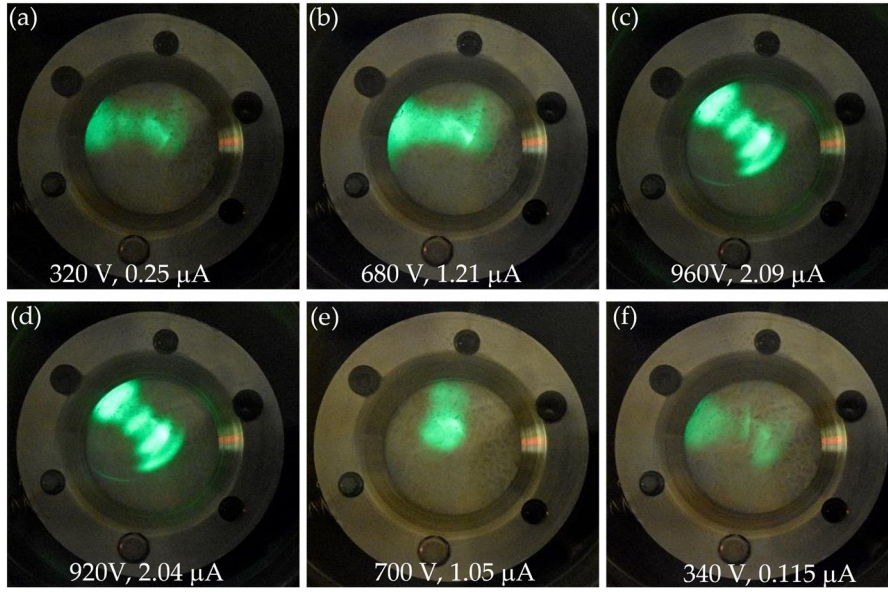
FIG. 15. FEM pattern images for the coated Mo$_2$. The images were captured at different current-voltage data as presented in each part (a)–(f).
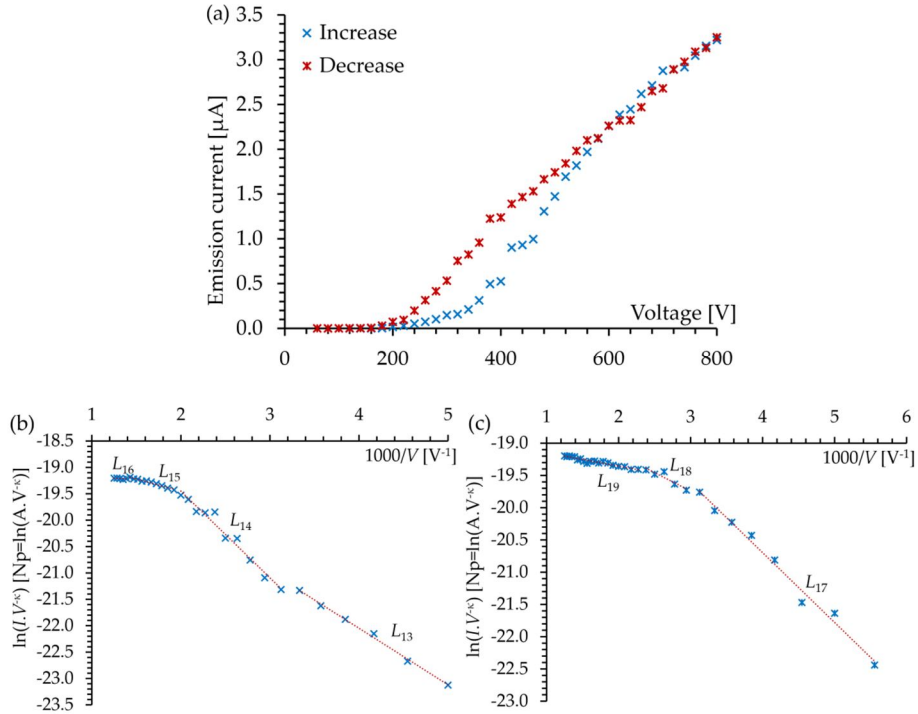
FIG. 16. The obtained (a) current-voltage characteristics for a full applied voltage cycle for the sample coated Mo$_2$, and the Murphy-Good plots for the (b) increasing and (c) decreasing parts of the cycle.

TABLE 4. Field emission orthodoxy test and field emission analysis results for the coated Mo$_2$ sample.

Segment	f_c		Test	A_f^{SN}	ζ_c
index L_i	f_c^{low}	f_c^{up}	result	[m^2]	[nm]
L_{13}	1.14	1.7	Fail	N/A	N/A
L_{14}	1.32	1.92	Fail	N/A	N/A
L_{15}	6.61	8.90	Fail	N/A	N/A
L_{16}	121.26	134.73	Fail	N/A	N/A
L_{17}	1.00	1.77	Fail	N/A	N/A
L_{18}	3.70	4.57	Fail	N/A	N/A
L_{19}	13.15	23.91	Fail	N/A	N/A

The decreasing part of the cycle was then performed until the threshold voltage was recorded at $V_{TH} = 120$ V with an emission current value of $I_{TH} = 0.021$ μA. The $I_m(V_m)$ in Fig. 16(a) shows the characteristics for both parts of the voltage cycle.

The related MG-plots are presented in Figs. 16(b)-16(c). The voltage increase part, as depicted in Fig. 16(b), contains four segments $(L_{13} - L_{16})$ and their analysis results are presented in Table 4. As for the voltage decrease part, depicted in Fig.16(c), the plot consists of three segments $(L_{17} - L_{19})$. For this sample, all the segments failed the orthodoxy test with high extracted scaled field values as expected and discussed earlier.

As a final remark on the MG-analysis results, the electrons were emitted by transmitting through the dielectric layer to the vacuum level, indicating more thermionic emission characteristics than field emission characteristics. This is believed to be the reason behind obtaining high extracted scaled field values even at lower operation voltages.

4. Conclusions

In the context of this study, the electrical properties of the Resinpal 2301 epoxy were obtained, including its surface chemical composition analysis, average local work function, and ionization energy.

The study included the description of a new methodology for preparing molybdenum single-tip field emitters. This was achieved by using a methanol and sulfuric acid solution in the electrochemical polishing technique instead of the sodium hydroxide solution.

Prepared molybdenum samples were coated with different thicknesses of the coating material. The resulting composite samples were tested, and their field emission performance was reported in comparison with their performance before applying the epoxy resin layer.

The results showed improved field emission characteristics for the case of composite samples: the electron beam was more condensed and brighter, the threshold voltage was much lower, and the operational voltage interval could be narrower with higher resulting current values. Table 5 shows comparative results between the two cases, the uncoated and coated molybdenum samples.

TABLE 5. field emission performance results of coated and uncoated molybdenum single-tip field emitters. The emission current is taken from the decreasing part of an applied voltage cycle.

Sample	Threshold voltage [V]			Emission current at 1 kV [μA]	
index Mo_i	uncoated (a)	coated (b)	a/b ratio	uncoated	coated
Mo_1	1080	180	600%	0.015	2.3
Mo_2	720	400	180%	0.14	1.5
Mo_3	760	320	237.5%	0.05	2.5
Mo_4	1640	120	1366%	0	$I > 3$

The Murphy-Good analysis for the uncoated molybdenum showed higher voltage conversion length values than in the case of tungsten, where these values usually fall within the range of 180-240 nm. This means that molybdenum has a more uniform surface electrostatic field that extends over a greater distance from its surface. Also, molybdenum showed lower formal emission areas compared to tungsten. As a final remark, it is strongly recommended to apply the Resinpal 2301 epoxy resin as a coating material for molybdenum single-tip field emitters in field emission-related experiments.

References

[1] Kyritsakis, A. and Xanthakis J.P., Proc. R. Soc. A, 471 (2014) 20140811.

[2] Holgate, J.T. and Coppins, M., Phys. Rev. Appl., 7 (2017) 044019.

[3] Allaham, M.M., Forbes, R.G., Knápek, A., Sobola, D., Burda, D., Sedlák, P. and Mousa M.S., Mater. Today Commun., 31 (2022) 103654.

[4] Murphy, E.L. and Good, R.H., Phys. Rev., 102 (1956) 1464.

[5] Jensen, K.L., "Introduction to the Physics of Electron Emission", (John Wiley and Sons, UK, 2018).

[6] Forbes, R.G., Roy. Soc. Open Sci., 6 (2019) 190912.

[7] Alabth, M., Shatnawi, M.T.M., Allaham, M.M. and Mousa, M.S., Ultramicroscopy, 244 (2023) 1134643.

[8] Filipov, S.V., Kolosko, A.G., Popov, E.O. and Forbes, R.G., R. Soc. Open Sci., 9 (2022) 220748.

[9] Madanat, M., Al-Tabbakh, A.A., Alsa'eed, M., Al-Dmour, H. and Mousa, M.S., Ultramicroscopy, 234 (2022) 113479.

[10] Allaham, M.M., Forbes, R.G., Knápek, A. and Mousa M.S., J. Electr. Eng. Slovak, 31 (2020) 37.

[11] Popov, E.O., Filipov, S.V., Kolosko, A.G. and Knápek, A., J. Vac. Sci. Technol. B, 40 (2022) 024201.

[12] Madanat, M., Al Sahre, M., Allaham, M.M. and Mousa, M.S., J. Vac. Sci. Technol. B, 39 (2021) 024001.

[13] Forbes, R.G., Proc. R. Soc. Lond. A, 469 (2013) 20130271.

[14] Burda, D., Allaham, M.M., Knápek, A., Sobola, D. and Mousa, M.S., 34th IVNC, France (2021).

[15] Mousa, M.S. and Kelly, T., Ultramicroscopy, 95 (2003) 125.

[16] Al-Qudah, A.M., Alnawasreh, S.S., Madanat, M., Trzaska, O., Matykiewicz, D., Alrawshdeh, S.S., Hagmann, M.J. and Mousa, M.S., Jordan J. Phys., 11(1) (2018) 59.

[17] Filip, V., Nicolaescu, D., Okuyama, F., Plavitu, C.N. and Ithoh, J., Appl. Surf. Sci., 146 (1999) 347.

[18] Filip, V., J. Vac. Sci. Technol. B, 17 (1999) 520.

[19] Al Soud, A., Knápek, A. and Mousa, M.S., Jordan J. Phys., 13 (3) (2020) 191.

[20] Al Soud, A., Al Buqain, R.N. and Mousa, M.S., Jordan J. Phys., 13 (3) (2020) 253.

[21] Alnawasreh, S.S., Al-Qudah, A.M., Madanat, M.A., Bani Ali, E.S., Almasri, A.M. and Mousa, M.S., Appl. Microsc., 46 (4) (2016) 227.

[22] Latham, R.V. and Mousa, M.S., Appl. Phys., 19 (1986) 699.

[23] Walker, P. and Tarn, W.H., "CRC Handbook of Metal Etchants". (CRC press, 1990).

[24] Knápek, A., Sýkora, J., Chlumská, J. and Sobola, D., Microelectron. Eng., 173 (2017) 42.

[25] Shao, G., Energy Environ. Mater., 4 (3) (2021) 273.